Extreme shifts in pyrite sulfur isotope compositions reveal the path to bonanza gold

Duncan F. McLeish[a,b,1] (ID), Anthony E. Williams-Jones[a] (ID), James R. Clark[a], and Richard A. Stern[c]

Pyrite is the most common sulfide mineral in hydrothermal ore-forming systems. The ubiquity and abundance of pyrite, combined with its ability to record and preserve a history of fluid evolution in crustal environments, make it an ideal mineral for studying the genesis of hydrothermal ore deposits, including those that host critical metals. However, with the exception of boiling, few studies have been able to directly link changes in pyrite chemistry to the processes responsible for bonanza-style gold mineralization. Here, we report the results of high-resolution secondary-ion mass spectrometry and electron microprobe analyses conducted on pyrite from the Brucejack epithermal gold deposit, British Columbia. Our $\delta^{34}S$ and trace element results reveal that the Brucejack hydrothermal system experienced abrupt fluctuations in fluid chemistry, which preceded and ultimately coincided with the onset of ultra-high-grade mineralization. We argue that these fluctuations, which include the occurrence of extraordinarily negative $\delta^{34}S$ values (e.g., –36.1‰) in zones of auriferous, arsenian pyrite, followed by sharp increases of $\delta^{34}S$ values in syn-electrum zones of nonarsenian pyrite, were caused by vigorous, fault valve-induced episodic boiling (flashing) and subsequent inundation of the hydrothermal system by seawater. We conclude that the influx of seawater was the essential step to forming bonanza-grade electrum mineralization by triggering, through the addition of cationic flocculants and cooling, the aggregation of colloidal gold suspensions. Moreover, our study demonstrates the efficacy of employing high-resolution, in situ analytical techniques to map out individual ore-forming events in a hydrothermal system.

gold | Brucejack deposit | pyrite chemistry | epithermal systems | nanoparticles

With global concern regarding the availability of energy- and technology-critical elements to empower the transition to a sustainable, clean-energy economy, increased attention is being given to epithermal gold deposits because they are the source of many critical metals (e.g., tellurium, selenium, and antimony) recovered as by-products of gold mining (1–4). However, despite this increased interest, the genesis of ultra-high-grade "bonanza"-type hydrothermal deposits (i.e., those with localized metal concentrations many orders of magnitude greater than the average) remains enigmatic. This paper deals with bonanza-type epithermal deposits, which recent research indicates form via the physical transport of metals in the solid state as colloidal suspensions instead of dissolved species (5–7). Similar findings have also recently been reported for other deposit types (e.g., orogenic 8–10; Carlin-type 11). This wave of research into nanoscale processes has been propelled by earlier investigations that 1) established the existence of colloidal gold particles in fossil hydrothermal systems through nanoscale imaging (12–15) and 2) detected their presence in active geothermal systems by microscale imaging and microanalytical means (16–18). Such advances have collectively demonstrated the need to look beyond traditional genetic models of aqueous complexation, i.e., those invoking the transport of gold in solution (e.g., refs. 19–23), to explain the formation of bonanza-type epithermal gold deposits. They have also validated the idea, first proposed 100 y ago (24, 25), that colloidal gold suspensions may play an important role in the formation of hydrothermal gold deposits.

Although recent research has established the existence of colloidal gold particles in hydrothermal ore-forming systems, a separate but equally essential question for colloid-based genetic models that remains largely unresolved is, what triggers flocculation, i.e., the formation of masses of solid gold through the aggregation of colloidal particles? Previous studies investigating this question have focused on a subset of bonanza-type hydrothermal gold deposits in which colloidal gold is believed to have developed within a silica gel, and aggregation occurred through the expulsion of the gold nanoparticles from the silica gel during its crystallization to quartz (26, 27). The causes of flocculation, however, extend well beyond processes related to quartz crystallization from silica gels, given that 1) flocculated gold nanoparticles have been documented in nonsilicate minerals (e.g., calcite) in the absence of quartz (6); and 2) the propensity of gold nanoparticles in laboratory experiments to kinetically self-aggregate in

Significance

Colloidal gold particles are increasingly recognized as playing a key role in the formation of hyperenriched, "bonanza"-type hydrothermal gold deposits. Despite a growing body of evidence for their existence in fossil hydrothermal and active geothermal systems, relatively little is known about the processes that cause these particles to flocculate and form discrete occurrences of ultra-high-grade gold. Here, we report evidence for a unique gold nanoparticle flocculation mechanism preserved in the largest and finest scale intragrain variations in pyrite sulfur isotope compositions ever identified in a nonbiogenic sulfide mineral. From this evidence, we demonstrate that the mixing of seawater with boiled ore fluid is an essential catalyst for gold nanoparticle flocculation and leads to the formation of bonanza-grade gold mineralization.

response to chemically triggered disruptions of their repulsive surface charges (28). Widely recognized mechanisms for forming precious metal ores from solution, such as boiling, fluid mixing, and reduction also have been proposed as triggers for flocculation (8, 15, 29), yet there is a lack of evidence that links these processes directly to bonanza-grade gold deposition.

To address this fundamental knowledge gap, we have undertaken a detailed sulfur isotope and trace element study of pyrite from the Brucejack epithermal gold deposit, a fossil hydrothermal system in northwestern British Columbia, Canada. Specifically, we have sought to elucidate the intragrain $\delta^{34}S$ isotopic and As–Au trace element record of pyrite that preceded, and ultimately coincided with, the formation of ultra-high-grade gold mineralization through flocculation of colloidal gold suspensions in a bonanza-type deposit. We studied pyrite because, being the only sulfide mineral to have formed throughout every major ore and alteration event in the paragenesis of the deposit, it is abundant and widespread (13, 30). Pyrite thus offers a unique and uninterrupted record of fluid evolution and insight into the physicochemical conditions that governed the flocculation of colloidal gold suspensions.

Pyrite and Fluid Evolution in Epithermal Ore Deposits

Owing to its ability to form over a wide range of physicochemical conditions, its abundance in most fossil hydrothermal systems, and its sensitivity to changes in fluid chemistry, pyrite has become widely recognized as an important monitor of fluid evolution in

ore deposits [see Steadman et al. (31) and Babedi et al. (32)]. Most studies of pyrite in epithermal deposits have focused on trace element distributions (e.g., Börner et al. 33), and some research has related these distributions and the microtextural characteristics of pyrite to ore-forming processes such as boiling (e.g., Román et al. 34). Although a few studies have investigated the intracrystalline isotopic changes that likely accompany, and may be characteristic of, major ore-forming events in porphyry-epithermal (e.g., Peterson & Mavrogenes 35) and Carlin-type deposits (e.g., Barker et al. 36), none have used such data to interpret the controls on bonanza gold mineralization.

The Brucejack Deposit

Brucejack is a large (15.7 million tons grading 8.4 ppm Au, 59.6 ppm Ag) intermediate-sulfidation Au–Ag epithermal deposit that hosts locally spectacular, bonanza-grade (up to 42,100 ppm Au in a 0.5 m drill core interval) gold mineralization (Fig. 1) (37). The gold occurs in carbonate–quartz vein swarms, fault-fill vein breccias, and stockworks in a phyllically altered Early Jurassic succession of intermediate to mafic fragmental volcanic and volcaniclastic host rocks that extends over a vertical interval of greater than 1 km (30, 38). Ore formation is estimated to have taken place in the temperature range of 160 to 200 °C (30, 39). The deposit was emplaced near the margin of the long-lived Stikinia island arc at ~184 Ma, shortly before it was intruded by a suite of 183 Ma intermediate to mafic dykes (38). Bonanza gold mineralization occurs primarily as 1 to 30 cm wide clots of calcite ± quartz-hosted dendritic electrum ($Au_{62}Ag_{38}$)
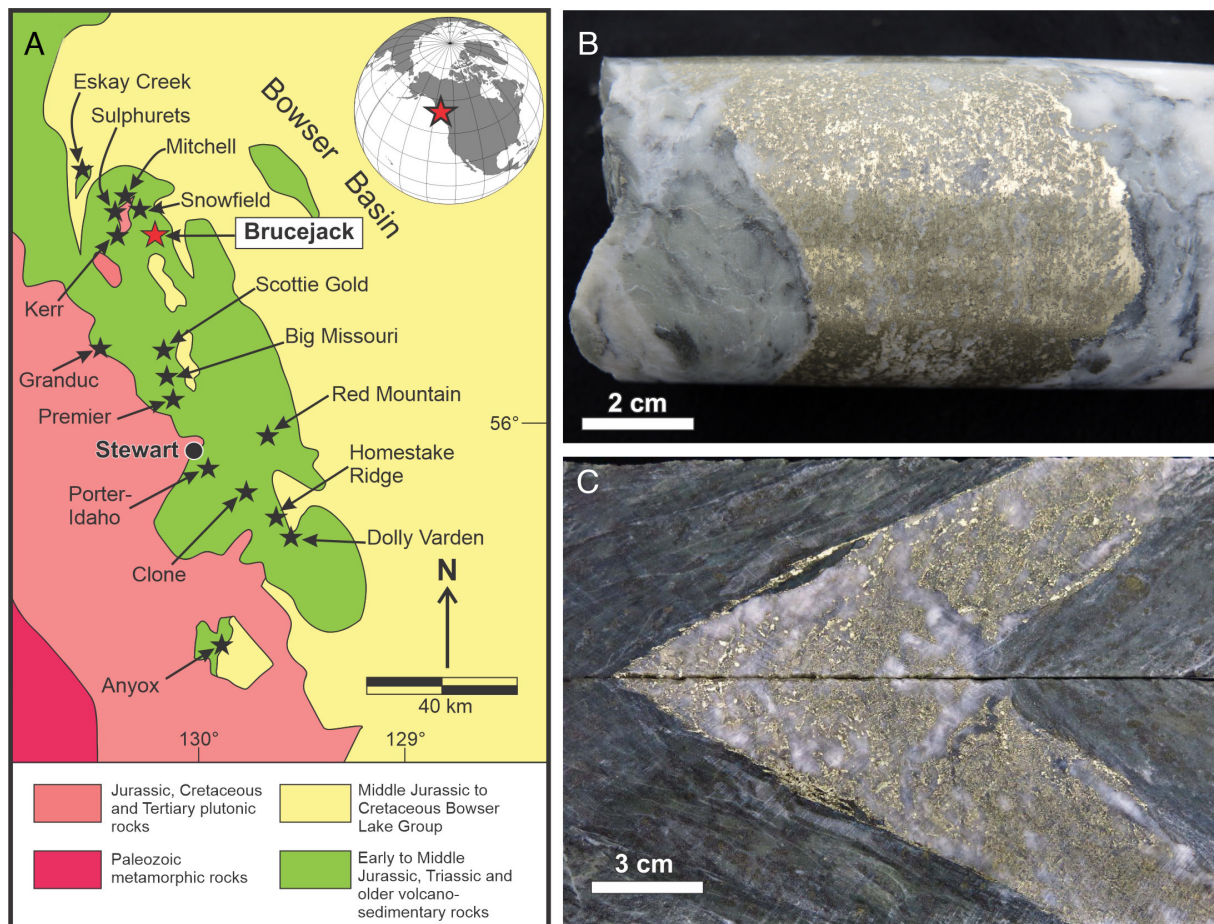

Fig. 1. (A) Location of the Brucejack deposit (red star) shown in relation to major hydrothermal ore deposits of the Stewart area, northwestern British Columbia. (B and C) bonanza-style gold mineralization in ultra-high-grade drill core samples from the Brucejack deposit (grading 42,100 and 27,100 ppm Au, respectively, over 0.5 m intervals).

which occurs commonly in contact with pyrite in three stages of ore veins (40). The ore-stage veins, which cross-cut two premineralization vein generations (stages I and II), form part of a broader, six-stage paragenetic sequence (30, 38) and include 1) quartz-carbonate ± sericite ± pyrite stockwork veins and breccias (stage III); 2) Zn–Pb–Fe–(Cu) quartz-sulfide veins (stage IV); and 3) Ca–Mn–Mg carbonate ± quartz ± pyrite veins locally containing distinctive orange-colored, Mn-bearing and gray-colored, Mg-bearing calcite (stage V; stage VI is postmineralization) (18). In addition to electrum, bonanza-grade silver mineralization also occurs locally as Ag–sulfosalts in stage IV veins (38).

Most vein-hosted pyrite at Brucejack is cross-cut by high-grade electrum and is therefore believed to have formed during an earlier alteration event which was widespread and consisted predominantly of quartz–sericite–pyrite replacement (phyllic alteration) of the wallrocks (40). Volumetrically minor, late-stage pyrite occurs in textural equilibrium with electrum and is interpreted to have formed during emplacement of the three main electrum-hosting vein stages (stages III–V) (30, 38, 39). Both wallrock- and vein-hosted pyrite exhibit multiphase growth zoning including 1) cubic cores with elevated Ni, Se, Sb, Co, Pb, and Bi concentrations, surrounded by 2) oscillatory zones containing alternating high/low As ± Au growth bands and locally well-developed colloform textures and 3) an outermost cubic growth zone that lacks trace-element zonation (39). Strong similarities in the trace element distributions of the first two growth phases of vein-hosted pyrite and those of pyrite in the wallrock suggest that these components were inherited from the wallrocks (40).

Although the origin of the gold mineralization at Brucejack is not completely understood, a recent study has provided evidence that a substantial proportion of the gold was transported mechanically in the solid state to the site of deposition as colloidal suspensions (6). In particular, transmitted electron microscopy imaging of bonanza-grade gold samples from the deposit has shown that 1) gold commonly occurs as <1 to 10 nm spherical nanocrystals of electrum embedded within a calcite matrix; 2) larger (100 to 500 nm) particles of electrum, also embedded in calcite, are composed of hundreds of nanoparticles, each displaying distinct crystal lattice plane orientations; and 3) the margins of >1-μm-wide electrum masses surrounding the calcite matrix comprise nanoparticulate electrum partially crystallized to massive monocrystalline electrum. The textures captured in these images have provided direct evidence for the involvement of colloidal gold particles in the formation of bonanza gold occurrences through flocculation.

Methods

We sampled pyrite from the three stages of electrum-bearing veins as well as preelectrum phyllic wallrock alteration from the Brucejack mine to investigate the trace element and $\delta^{34}S$ intragrain isotopic record that preceded, and eventually coincided with, the formation of high-grade gold mineralization. An initial, qualitative survey of intragrain compositions was conducted on standard petrographic polished thin sections of the samples using energy-dispersive X-ray spectroscopy and was followed by the quantitative determination of element concentrations via electron microprobe (EMP) analysis. Sulfur isotope compositions were subsequently determined in situ by high-resolution secondary ion mass spectrometry (SIMS) analyses. The typical spot size used and maximum uncertainty (2σ) for the SIMS $\delta^{34}S$ analyses were 7 to 10 μm and 0.4‰ (typically ≤ 0.2 ‰), respectively. See *SI Appendix* for additional analytical details and complete results.

Results

Detailed backscattered electron (BSE) imaging of pyrite from mineralized veins and phyllically altered wallrock revealed two significant results. First, the previously reported three pyrite growth events (see

above) are present in samples from all vein stages and wallrock and, second, textures exhibited by the oscillatory-zoned arsenian bands from the intermediate growth event differ significantly from those of the other pyrite generations. For example, pyrite from the stage V, bonanza-grade Cleopatra vein in the core of the deposit (Valley of the Kings Zone), which has been a major source of gold production, is characterized by arsenian growth bands exhibiting locally well-developed colloform textures that become increasingly chaotic toward grain rims (Fig. 2*A*). In contrast, pyrite samples from phyllically altered wallrock directly adjacent to lower grade stage V veins near the periphery of the deposit display single, broad arsenian growth zones with sharp, euhedral outer limits (Fig. 3*A*). Analytical traverses across these two types of arsenian bands show that they are characterized by different sulfur isotope compositions (e.g., Figs. 2 vs. 3*A*; see *SI Appendix*, Fig. S1 for a detailed plot of As vs. $\delta^{34}S_{pyr}$ results). In the Cleopatra vein samples, colloform arsenian bands are associated with weakly to extremely negative $\delta^{34}S$ shifts (<1 to ~17‰ magnitude), whereas the euhedral arsenian bands in peripheral stage V veins are associated with $\delta^{34}S$ values that increase steadily from core to rim (from −1.3 to +24.0‰; Fig. 3*A* transect D–D'). Analyses of the colloform and euhedral arsenian bands indicate that the former hosts significant invisible Au (up to 150 ppm), whereas the latter contains no detectable Au (< ~90 ppm Au).

In addition to the $\delta^{34}S$ changes observed in the arsenian growth bands, the SIMS traverses demonstrate that many large intragrain $\delta^{34}S$ shifts, both negative and positive, occur in areas that otherwise lack compositional variation. For example, in the Cleopatra vein, pyrite transect B–B' (Fig. 2) exhibits several sharp drops in $\delta^{34}S$ in the first 300 μm that do not correlate with compositional changes evident from BSE imaging, and the outermost (grain rim) analyses show an extremely positive shift in a zone of nonarsenian pyrite. Similar positive shifts occur in the nonarsenian grain rims along traverses A–A' and C–C' (Fig. 2*B*). While the rim analyses in each traverse in Fig. 2 yielded variable $\delta^{34}S$ values, all traverses reveal an extremely positive $\delta^{34}S$ shift in the outermost growth zone which, importantly, is in textural equilibrium with high-grade electrum mineralization (El; Fig. 2).

In order to further explore the $\delta^{34}S$ shifts that led to the formation of electrum mineralization at Brucejack, a SIMS transect was made across a vein-margin-hosted pyrite grain from a second, stage V vein in the center of the deposit (Fig. 3*B*; E–E'). Along this transect, the vein-margin-parallel growth bands alternate between broad nonarsenian and narrow arsenian pyrite before terminating in an outer (i.e., toward the *Upper Left* of the image) zone of very small (<20 μm), isolated, and aggregated pyrite crystals. These small crystals have cubic to pyritohedron shapes and are in textural equilibrium with electrum, as is evidenced by the lack of reaction and/or replacement textures along the contacts between electrum and pyrite. The SIMS transect reveals two nonarsenian zones of pyrite with moderately positive $\delta^{34}S$ (+4 to +9‰) signatures, separated by a nonarsenian zone with near-zero $\delta^{34}S$ values. Beyond the nonarsenian zone, which terminates with a $\delta^{34}S$ of +3.8 (Fig. 3*B*; E–E'), there is a precipitous drop in $\delta^{34}S$ to a value of −36.1‰ over ~50 μm. This steep decline in $\delta^{34}S$ values coincides initially with a zone of arsenian pyrite and continues outward through a zone of nonarsenian pyrite. Moving further outward toward the contact with electrum, $\delta^{34}S$ values reverse sharply and increase by ~30‰ over a distance of ~30 μm through both arsenian and nonarsenian zones.

Discussion

The $\delta^{34}S$ traverses reported in this study record the largest intragrain variations in sulfur isotope compositions ever identified in a nonbiogenic sulfide mineral. For example, the range in $\delta^{34}S$
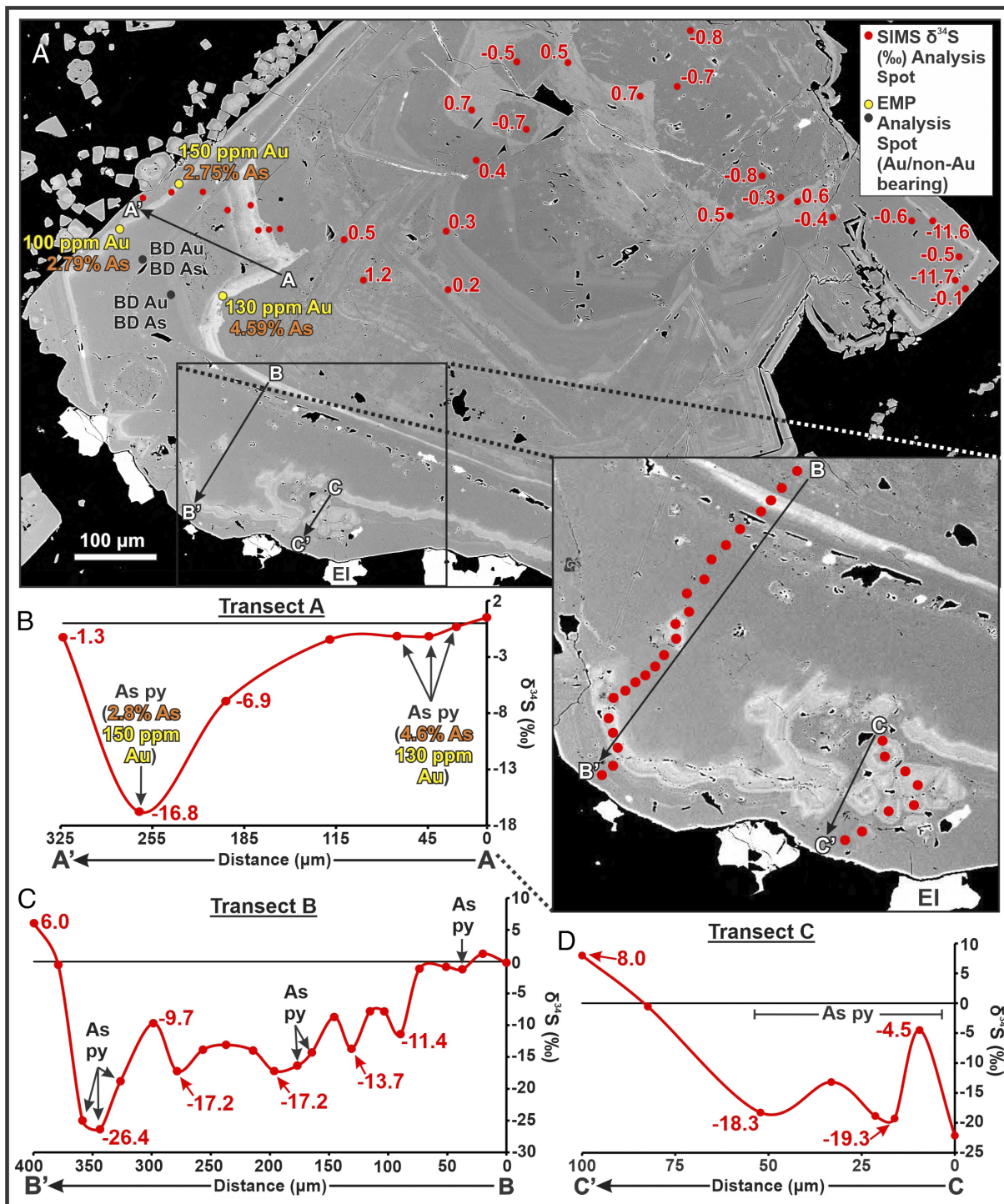
Fig. 2. (*A*) BSE image of pyrite and electrum (El) from the stage V Cleopatra vein showing complex, multigenerational growth zoning and the location of SIMS δ^{34}S analytical transects A–A', B–B', and C–C', as well as SIMS δ^{34}S results for analyses outside of the transects and EMP results for Au and As (BD = below detection). The electrum is interpreted to be in textural equilibrium with the outermost pyrite growth zone based on the lack of reaction and/or replacement textures along the contacts between the electrum and pyrite which are sharp and largely euhedral. (*B–D*) plots of δ^{34}S$_{pyr}$ vs. distance for transects A–A', B–B', and C–C', respectively.

values for a single Brucejack pyrite crystal, from +8.7 to –36.1‰ (Fig. 3*B*), far exceeds the largest previously reported single-crystal variations of +0.3 to –12.0‰ for pyrite from an epithermal deposit (35). Furthermore, the most negative δ^{34}S$_{pyr}$ value at Brucejack (–36.1‰; Fig. 3*B*) is substantially lower than even 1) the lowest δ^{34}S$_{pyr}$ values reported for a porphyry-epithermal deposit (41); or 2) the typical δ^{34}S for pyrite formed during open system bacterial reduction of marine sulfate (42). The extremely negative values at Brucejack, which are characterized by abrupt changes in pyrite growth, are almost certainly the product of rapid

boiling, as is interpreted for similar hydrothermal ore-forming systems (34, 43). By progressively releasing hydrogen to the vapor, boiling oxidized the hydrothermal liquid and caused extreme Rayleigh fractionation of isotopically heavier sulfur into sulfate and lighter sulfur into the reduced sulfur that formed the pyrite. This interpretation is supported by 1) the observation that the most negative δ^{34}S values occur in colloform arsenian pyrite, the texture and Au–As composition of which are typical of boiling-induced formation (34), and 2) evidence from the detailed study of fluid inclusions at Brucejack which indicates that the ore fluid
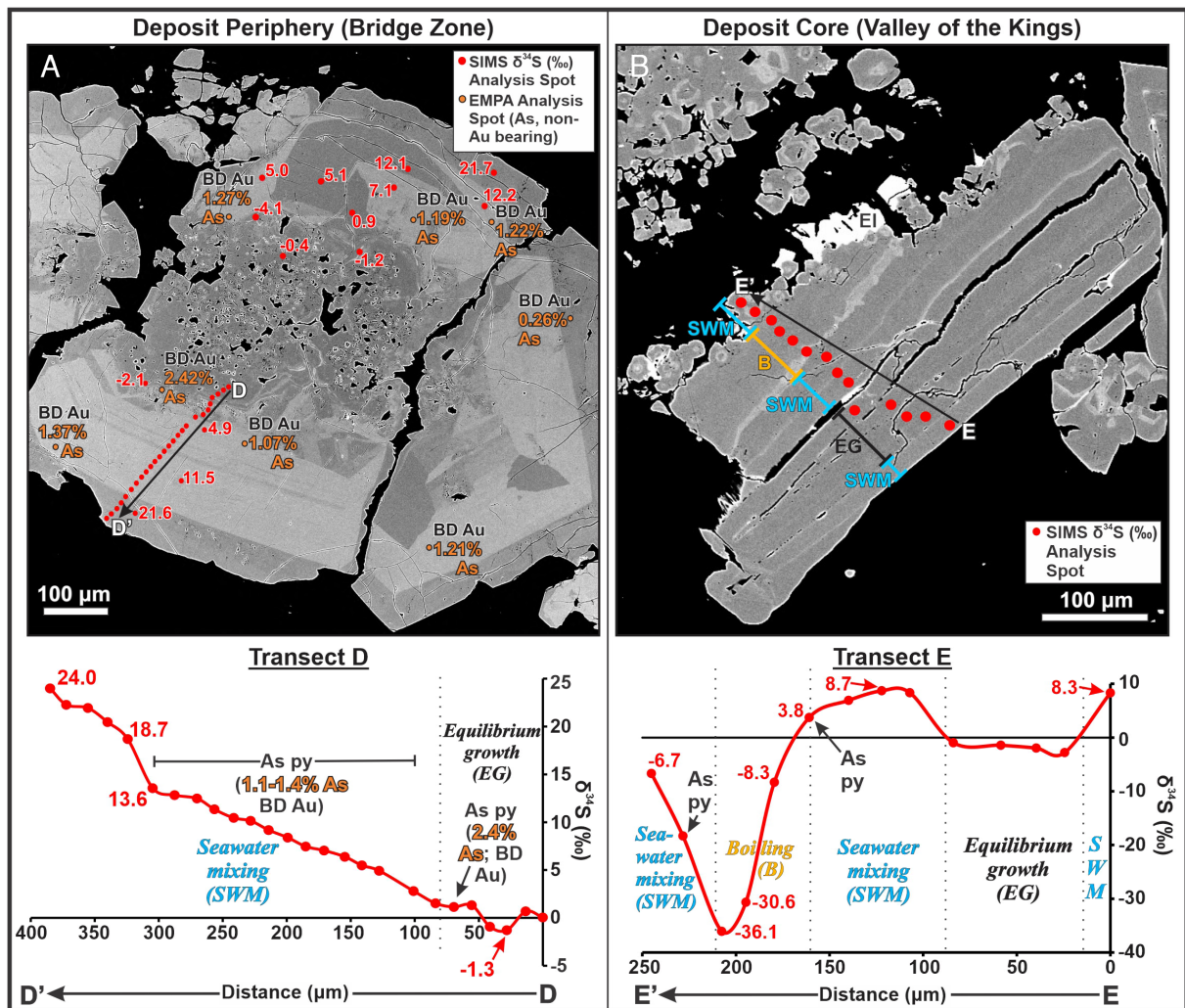
Fig. 3. (A) BSE image and corresponding SIMS $\delta^{34}S$ results for transect D–D′, and analysis spots outside the transect, for pyrite in a stage V vein from the deposit periphery; EMP analysis locations and corresponding As values are also shown (Au values are all below detection; BD). (B) BSE image of pyrite and adjacent electrum (El) in a stage V vein from the core of the deposit showing SIMS $\delta^{34}S$ results for transect E–E′.

boiled during the formation of stage III and V veins (30). Other hypotheses that have been proposed to explain strongly negative $\delta^{34}S$ values in auriferous, arsenian pyrite are cooling of highly oxidized magmatic fluids and/or extreme disproportionation of SO_2 (35, 44). In principle, these hypotheses could explain the very negative $\delta^{34}S$ values observed at Brucejack, but they are not credible because no $\delta^{34}S$ values <−25 ‰ have ever been reported for magmatic hydrothermal systems, even those evolving to very low temperature.

Although the large negative excursion of the pyrite $\delta^{34}S$ values at Brucejack is extraordinary, it is not the most noteworthy finding of this study. Even more surprising are the strongly positive $\delta^{34}S$ shifts that are texturally associated with electrum. They indicate that a process other than boiling must have been operating during bonanza gold deposition. The steady increase in $\delta^{34}S_{pyr}$ from near zero to ~+24‰ in the lower grade stage V peripheral veins (Fig. 3A) suggests that there was extensive mixing between an originally magmatic-dominant fluid and one with a substantially more positive $\delta^{34}S$ signature. Given that 1) the Brucejack deposit was emplaced near the edge of an Early Jurassic island arc undergoing widespread denudational extension and/or transtension (45, 46), and 2) Early Jurassic seawater was characterized by $\delta^{34}S$ values of +15 to 24‰ (47), we propose that this isotopically more positive fluid was seawater. Higher $\delta^{34}S_{pyr}$ values would have been

generated by the mixing of seawater-sourced sulfur produced in part by thermochemical sulfate reduction (TSR), a process that also precipitates carbonate and may explain the abundance of calcite around flocculated electrum at Brucejack (48). In VMS deposits formed at the seafloor–seawater interface, similar, positive intragrain $\delta^{34}S$ excursions (~20‰) have been documented in pyrite and attributed, in part, to TSR (49).

In addition to raising the $\delta^{34}S$ values of the hydrothermal fluids circulating at Brucejack, inundation of the hydrothermal system by seawater added cationic flocculants, primarily Na^+, but also Mg^{2+}, Ca^{2+}, and K^+ (50). Although the initial Mg^{2+}, Ca^{2+}, and K^+ concentrations of the Brucejack ore fluid have not been constrained, a fluid inclusion study by Tombe et al. (30) suggested that the electrum-bearing stage V ore veins at Brucejack have salinity values that are largely below those of Early Jurassic seawater [~4.3 wt % NaCl (51)]. Thus, this mixing would have effectively increased the concentration of background electrolyte and the ionic strength of the ore fluid (52), resulting in the adsorption of cations onto the surfaces of the negatively charged gold nanoparticles (53) being transported in suspension in the fluid (Fig. 4). The adsorbed cations, which protruded outward from nanoparticle surfaces, attached to the adjacent gold nanoparticles and triggered bridging flocculation (52) of colloidal gold suspensions at seawater mixing sites in the Brucejack hydrothermal system. The elevated
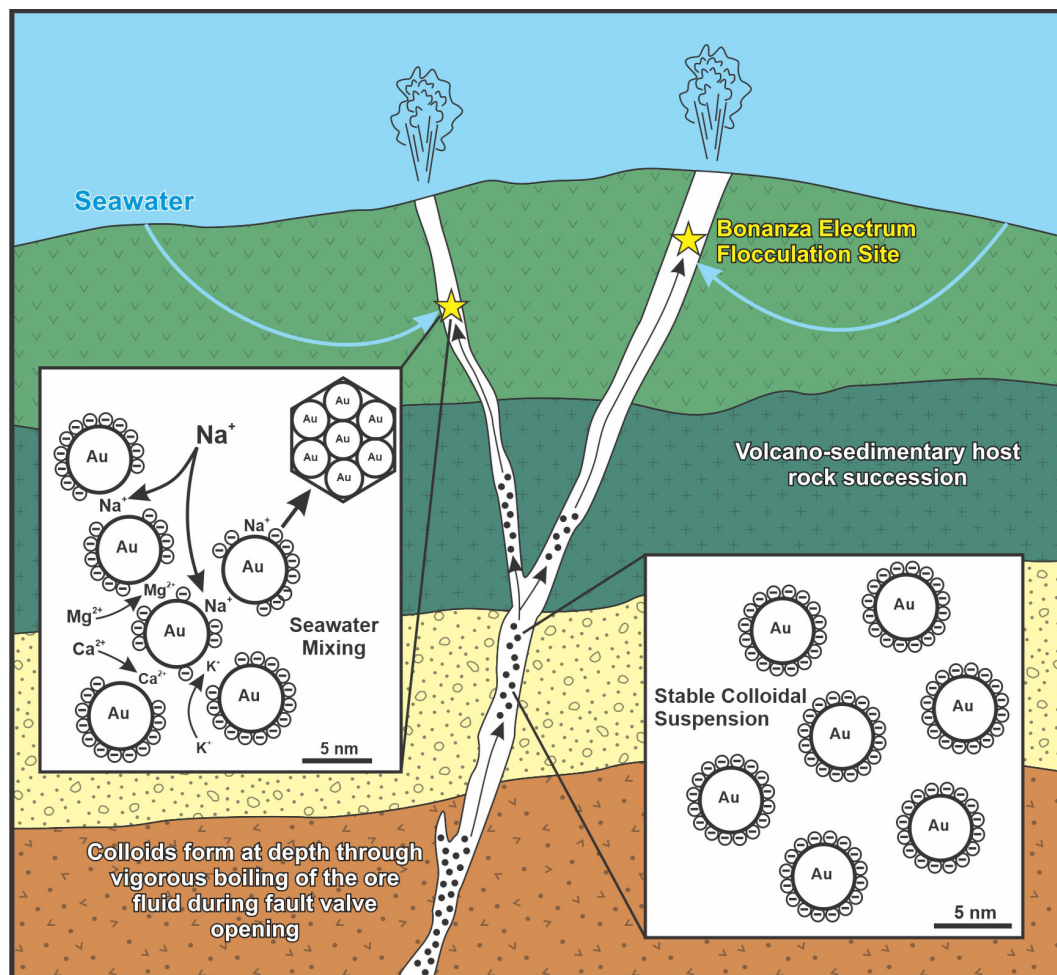
Fig. 4. Schematic model for the formation of hydrothermal bonanza gold mineralization by seawater-induced flocculation of colloidal gold suspensions. See text for further discussion.

background electrolyte concentration in the seawater–ore fluid mixture further promoted bridging flocculation by increasing the compression of the electric double layer around the gold nanoparticles. This brought the suspended gold nanoparticles closer together because of the screening of their repulsive surface charges (52). Though some flocculated gold particles may have deposited at the fluid mixing sites, seismic pumping (see below) likely circulated most of the flocculated gold aggregations to other sites in the deposit, where they locally clogged fractures and ultimately formed clots of bonanza-style gold mineralization through the repetitive addition of flocculated gold aggregates (6).

Integration of the Brucejack intragrain $\delta^{34}S_{pyr}$ record across the deposit reveals a complex interplay of processes leading to, and culminating in, the formation of bonanza gold mineralization (Fig. 4). The cyclical, progressively more negative, and extreme shifts in $\delta^{34}S$ values in the ultra-high-grade Cleopatra vein (Fig. 2) reflect multiple boiling events which became incrementally more intense over time and may have been responsible for the nucleation of the colloidal gold particles which later flocculated during seawater mixing. This cyclical boiling, which is consistent with a seismic pumping fault-valve model (54), terminated in a singular extreme boiling event that depressed the $\delta^{34}S$ signature by ~17‰ prior to seawater mixing and the onset of bonanza-style mineralization. Fig. 3 demonstrates that pyrite in other high-grade veins, while recording a similarly extreme terminal boiling event followed by a sharp syn-electrum increase in $\delta^{34}S$, preserves an earlier history of the mixing of the ore fluid with seawater unseen

by the Cleopatra vein. In transect E–E', $\delta^{34}S$ values in pyrite were initially below the range for equilibrium with Early Jurassic seawater. We speculate that the moderately positive $\delta^{34}S$ signature (+8.7‰) from this transect reflects the initial onset of fault-valve-induced seawater–ore fluid mixing.

In closing, our findings have fundamental implications for the processes by which bonanza-grade hydrothermal gold deposits form, and demonstrate how grain-scale microtextural and mineral chemical analyses can be used to assess mineralization processes. First, by establishing the synchronous nature of fluid-mixing and high-grade mineralization in a deposit where colloidal transport of gold has been identified (6), this study provides direct evidence for syn-mineralization seawater-mixing, a process that may drive the flocculation of gold nanoparticles. Second, contrary to Weatherley & Henley (55), our results are consistent with the idea that the sulfur isotopic compositions of sulfide minerals record the primary physicochemical changes associated with rapid boiling events. Third, the $\delta^{34}S$ transects presented here indicate that, although the occurrence of colloform arsenian pyrite is indeed due to boiling, "invisible" boiling events, i.e., those with no obvious textural or mineral-chemical record, can be relatively common (e.g., transect B–B', Fig. 2). Fourth, our findings highlight the importance of using in situ analytical techniques to resolve stable isotope signatures at the micron-scale; previous studies at Brucejack using whole-grain analytical methods yielded fairly consistent $\delta^{34}S$ values for pyrite from mineralized veins, in a narrow range of –1.7 to +0.6‰ (30), which are clearly misleading. Fifth, although the

EMP data presented here and elsewhere (40) provide compelling evidence that boiling was accompanied by significant deposition of gold in the form of auriferous pyrite, the positive, seawater-driven, syn-electrum $\delta^{34}S$ shifts in Brucejack pyrite strongly suggest that fluid mixing was the ultimate trigger for high-grade gold mineralization. Finally, as exploration models for bonanza-type epithermal gold deposits have been developed almost exclusively for subaerial environments (e.g., refs. 56 and 57), our finding of a seawater-related mechanism for bonanza gold deposition highlights the need to refine the existing exploration models to recognize ore-forming processes that are unique to submarine settings.

Data, Materials, and Software Availability. All study data are included in the article and/or *SI Appendix*.

Author affiliations: [a]Department of Earth and Planetary Sciences, McGill University, Montréal, QC H3A 0E8, Canada; [b]Newmont Corporation, Vancouver, BC V6E 3X2, Canada; and [c]Department of Earth and Atmospheric Sciences, University of Alberta, Edmonton, AB T6G 2E3, Canada

1. R. J. Goldfarb, A. H. Hofstra, S. F. Simmons, "Critical elements in Carlin, epithermal, and orogenic gold deposits" in *Rare Earth and Critical Elements in Ore Deposits*, P. L. Verplanck, M. W. Hitzman, Eds. (Society of Economic Geologists, 2016), pp. 217–244.
2. S. M. Jowitt *et al.*, "The critical metals: An overview and opportunities and concerns for the future" in *Metals, Minerals, and Society*, A. M. Arribas, J. L. Mauk, Eds. (Society of Economic Geologists, 2018), pp. 25–38.
3. Final List of Critical Minerals, Interior Releases 2018's Final List of 35 Minerals Deemed Critical to U.S. National Security and the Economy. USGS. https://www.usgs.gov/news/national-news-release/interior-releases-2018s-final-list-35-minerals-deemed-critical-us. Accessed 27 August 2023.
4. G. M. Mudd *et al.*, "Critical Minerals in Australia: A Review of Opportunities and Research Needs" (Tech. Rep. 2018/51, Geoscience Australia, Canberra, 2018).
5. J. A. Saunders, M. Burke, M. E. Brueseke, Scanning-electron-microscope imaging of gold (electrum) nanoparticles in middle Miocene bonanza epithermal ores from northern Nevada, USA. *Miner. Deposita* **55**, 389–398 (2020).
6. D. F. McLeish, A. E. Williams-Jones, O. V. Vasyukova, J. R. Clark, W. S. Board, Colloidal transport and flocculation are the cause of the hyper-enrichment of gold in nature. *Proc. Natl. Acad. Sci. U.S.A.* **118**, e2100689118 (2021), 10.1073/pnas.2100689118.
7. N. Cano *et al.*, Nanomaterial accumulation in boiling brines enhances epithermal bonanzas. *Sci. Rep.* **13**, 14985 (2023).
8. L. Petrella *et al.*, Colloidal gold transport, a key to high-grade gold mineralization? *Miner. Deposita* **55**, 1247–1254 (2020).
9. C. R. Voisey *et al.*, Aseismic refinement of orogenic gold systems. *Eco. Geol.* **115**, 33–50 (2020).
10. E. C. G. Hastie, M. Schindler, D. J. Kontak, B. Lafrance, Transport and coarsening of gold nanoparticles in an orogenic deposit by dissolution–reprecipitation and Ostwald ripening. *Commun. Earth Environ.* **2**, 57 (2021).
11. J. Yan, R. Hu, J. S. Cline, S. Fu, S. Liu, SEM and FIB-TEM analyses on nanoparticulate arsenian pyrite: Implications for Au enrichment in the Carlin-type giant Lannigou gold deposit, SW China. *Am. Mineral.* **109**, 215–224 (2024).
12. M. L. Burke, "An electron microscopy investigation of gold and associated minerals from round mountain, Nevada", MSc thesis, Miami University, Oxford, OH (2015), p. 59.
13. N. J. Harrichhausen, "Role of colloidal transport in the formation of high-grade gold veins at Brucejack, British Columbia", MSc thesis, McGill University, Montreal, QC, Canada (2016).
14. M. Burke, J. Rakovan, M. P. S. Krekeler, A study by electron microscopy of gold and associated minerals from Round Mountain, Nevada. *Ore Geol. Rev.* **91**, 708–717 (2017).
15. J. A. Saunders, M. Burke, Formation and aggregation of gold (electrum) nanoparticles in epithermal ores. *Minerals* **7**, 163 (2017), 10.3390/min7090163.
16. M. Hannington, V. Harðardóttir, D. Garbe-Schönberg, K. L. Brown, Gold enrichment in active geothermal systems by accumulating colloidal suspensions. *Nat. Geosci.* **9**, 299–302 (2016).
17. A. Gartman *et al.*, Boiling-induced formation of colloidal gold in black smoker hydrothermal fluids. *Geology* **46**, 39–42 (2018).
18. M. Hannington, D. Garbe-Schönberg, Detection of gold nanoparticles in hydrothermal fluids. *Econ. Geol.* **114**, 397–400 (2019).
19. H. C. Helgeson, R. M. Garrels, Hydrothermal transport and deposition of gold. *Eco. Geol.* **63**, 622–635 (1968).
20. R. E. Krupp, T. M. Seward, The Rotokawa geothermal system, New Zealand; an active epithermal gold-depositing environment. *Eco. Geol.* **82**, 1109–1129 (1987).
21. A. Stefánsson, T. M. Seward, Gold (I) complexing in aqueous sulphide solutions to 500 C at 500 bar. *Geochim. Cosmochim. Acta* **68**, 4121–4143 (2004).
22. S. F. Simmons, K. L. Brown, Gold in magmatic hydrothermal solutions and the rapid formation of a giant ore deposit. *Science* **314**, 288–291 (2006).
23. N. C. Hurtig, A. E. Williams-Jones, An experimental study of the transport of gold through hydration of AuCl in aqueous vapour and vapour-like fluids. *Geochim. Cosmochim. Acta* **127**, 305–325 (2014).
24. H. C. Boydell, *The Role of Colloidal Solutions in the Formation of Mineral Deposits* (Institution of Mining and Metallurgy Transactions, 1924), vol. 36, pp. 145–337.
25. W. Lindgren, Gel replacement, a new aspect of metasomatism. *Proc. Natl. Acad. Sci. U.S.A.* **11**, 5–11 (1925).
26. R. J. Herrington, J. J. Wilkinson, Colloidal gold and silica in mesothermal vein systems. *Geology* **21**, 539–542 (1993).
27. L. Petrella *et al.*, Nanoparticle suspensions from carbon-rich fluid make high-grade gold deposits. *Nat. Commun.* **13**, 3795 (2022).
28. D. A. Weitz, M. Oliveria, Fractal structures formed by kinetic aggregation of aqueous gold colloids. *Phys. Rev. Lett.* **52**, 1433 (1984).
29. J. A. Saunders, Colloidal transport of gold and silica in epithermal precious-metal systems: Evidence from the Sleeper deposit, Nevada. *Geology* **18**, 757–760 (1990).
30. S. P. Tombe *et al.*, Origin of the high-grade early Jurassic Brucejack epithermal Au-Ag deposits, sulphurets mining camp, Northwestern British Columbia. *Ore Geol. Rev.* **95**, 480–517 (2018).
31. J. A. Steadman *et al.*, Pyrite trace element behavior in magmatic- hydrothermal environments: An LA-ICPMS imaging study. *Ore Geol. Rev.* **128**, 103878 (2021), 10.1016/j.oregeorev.2020.103878.
32. L. Babedi, B. P. von der Heyden, M. Tadie, M. Mayne, Trace elements in pyrite from five different gold ore deposit classes: A review and meta-analysis. *Geolog. Soc. Lond. Spl. Publ.* **516**, 47–83 (2022).
33. F. Börner *et al.*, Fingerprinting fluid evolution by trace elements in epithermal pyrite, Vatukoula Au-Te deposit, Fiji. *Ore Geol. Rev.* **137**, 104314 (2021), 10.1016/j.oregeorev.2021.104314.
34. N. Román *et al.*, Geochemical and micro-textural fingerprints of boiling in pyrite. *Geochim. Cosmochim. Acta* **246**, 60–85 (2019).
35. E. Peterson, J. A. Mavrogenes, Linking high-grade gold mineralization to earthquake-induced fault-valve processes in the Porgera gold deposit, Papua New Guinea. *Geology* **42**, 383–386 (2014).
36. S. L. L. Barker *et al.*, Uncloaking invisible gold: Use of NanoSIMS to evaluate gold, trace elements, and sulfur isotopes in pyrite from Carlin-type gold deposits. *Econ. Geol.* **104**, 897–904 (2009).
37. A. Shaw *et al.*, "Technical report on the Brucejack Gold Mine, Northwest British Columbia" (Tech. Rep. 220008-00-RPT-001, Tetra Tech Canada Inc., Vancouver, BC, Canada, 2020).
38. W. S. Board *et al.*, "The Brucejack Au-Ag deposit, northwest British Columbia, Canada: Multistage porphyry to epithermal alteration, mineralization, and deposit formation in an island-arc setting", H. Goldfarb *et al.*, Eds. (2020), pp. 289–311.
39. D. F. McLeish, "The nature and origin of the bonanza-grade Brucejack epithermal Au-Ag deposit, northwestern British Columbia," PhD thesis, McGill University, Montreal, Quebec, Canada (2022).
40. D. F. McLeish, A. E. Williams-Jones, W. S. Board, J. R. Clark, "Nature and origin of the Brucejack high-grade epithermal gold deposit, northwestern British Columbia (NTS 104B): 2017 update in Geoscience BC Summary of Activities 2017: Minerals and Mining Report 2018-1" (Tech. Rep. 2018-1, Geoscience, Vancouver, BC, Canada, 2018).
41. W. Hutchison, A. A. Finch, A. J. Boyce, The sulfur isotope evolution of magmatic-hydrothermal fluids: Insights into ore-forming processes. *Geochim. Cosmochim. Acta* **288**, 176–198 (2020).
42. D. E. Canfield, Isotope fractionation by natural populations of sulfate-reducing bacteria. *Geochim. Cosmochim. Acta* **65**, 1117–1124 (2001).
43. A. Schaarschmidt *et al.*, Boiling effects on trace element and sulfur isotope compositions of sulfides in shallow-marine hydrothermal systems: Evidence from Milos Island, Greece. *Chem. Geol.* **583**, 120457 (2021).
44. A. J. Wilson, D. R. Cooke, B. J. Harper, C. L. Deyell, Sulfur isotopic zonation in the Cadia district, southeastern Australia: Exploration significance and implications for the genesis of alkali porphyry gold-copper deposits. *Miner. Deposita* **42**, 465–487 (2007).
45. J. L. Nelson, J. Kyba, "Structural and stratigraphic control of porphyry and related mineralization in the Treaty Glacier–KSM–Brucejack–Stewart trend of northwestern Stikinia" in *Geological Fieldwork 2013* (2014), pp. 111–140, British Columbia Ministry of Energy, Mines and Petroleum Resources, 2014-1.
46. J. L. Nelson, B. van Straaten, R. Friedman, Latest Triassic-Early Jurassic Stikine–383 Yukon-Tanana terrane collision and the onset of accretion in the Canadian Cordillera: Insights from Hazelton Group detrital zircon provenance and arc–back-arc configuration. *Geosphere* **18**, 670–696 (2022).
47. A. Prokoph, G. A. Shields, J. Veizer, Compilation and time-series analysis of a marine carbonate δ18O, δ13C, 87Sr/86Sr and δ34S database through Earth history. *Earth Sci. Rev.* **87**, 113–133 (2008).
48. H. G. Machel, H. R. Krouse, R. Sassen, Products and distinguishing criteria of bacterial and thermochemical sulfate reduction. *Appl. Geochem.* **10**, 373–389 (1995).
49. A. J. Martin *et al.*, Mineral-scale variation in the trace metal and sulfur isotope composition of pyrite: Implications for metal and sulfur sources in mafic VMS deposits. *Miner. Deposita* **57**, 911–933 (2021).
50. M. Jeldres *et al.*, Copper tailing flocculation in seawater: Relating the yield stress with fractal aggregates at varied mixing conditions. *Metals* **9**, 1295 (2019).
51. W. W. Hay *et al.*, Evaporites and the salinity of the ocean during the Phanerozoic: Implications for climate, ocean circulation and life. *Palaeogeogr. Palaeoclimatol. Palaeoecol.* **240**, 3–46 (2006).
52. S. P. Yeap, J. Y. Sum, P. Y. Toh, Separation of nano-scaled particles by flocculation. *Chem. Eng. Technol.* **44**, 378–386 (2021).
53. R. K. Iler, *The Chemistry of Silica: Solubility, Polymerization, Colloid and Surface Properties and Biochemistry of Silica* (John Wiley & Sons, New York, 1979).
54. R. H. Sibson, J. M. Moore, A. H. Rankin, Seismic pumping–a hydrothermal fluid transport mechanism. *J. Geol. Soc.* **131**, 653–659 (1975).
55. D. Weatherley, R. W. Henley, Flash vaporisation during earthquakes evidenced by gold deposits. *Nat. Geosci.* **6**, 294–298 (2013).
56. R. H. Sillitoe, J. W. Hedenquist, "Linkages between volcanotectonic settings, ore-fluid compositions, and epithermal precious metal deposits" in *Volcanic, Geothermal, and Ore-Forming Fluids: Rulers and Witnesses of Processes Within the Earth*, S. F. Simmons, I. Graham, Eds. (Society of Economic Geologists, Special Publication 10, 2003), pp. 315–343.
57. L. Wang, K. Z. Qin, G. X. Song, G. M. Li, A review of intermediate sulfidation epithermal deposits and subclassification. *Ore Geol. Rev.* **107**, 434–456 (2019).